Wave Motion 137 (2025) 103542

Contents lists available at ScienceDirect

Wave Motion

journal homepage: www.elsevier.com/locate/wamot

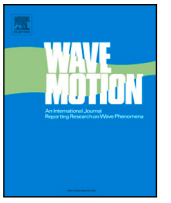

Impact of directional spreading on nonlinear KdV-soliton spectra in intermediate water

Yu-Chen Lee [a,*], Sander Wahls [b]

[a] Delft Center for Systems and Control, Mechanical Engineering, Delft University of Technology, Mekelweg 5, Delft, 2628 CD, South Holland, The Netherlands

[b] Karlsruhe Institute of Technology, Institute of Industrial Information Technology, Hertzstraße 16, Karlsruhe, 76187, Baden-Württemberg, Germany

ARTICLE INFO

Keywords:
Solitons
Korteweg–De Vries equation
Shallow water waves
Nonlinear Fourier transform
Directional spreading

ABSTRACT

The Korteweg–De Vries (KdV) equation is a partial differential equation used to describe the dynamics of water waves under the assumptions of shallow water, unidirectionality, weak nonlinearity and constant depth. It can be solved analytically with a suitable nonlinear Fourier transform (NFT). The NFT for the KdV equation is subsequently referred to as the KdV-NFT. The soliton part of the nonlinear Fourier spectrum provides valuable insights into the nonlinear evolution of waveforms by exposing the amplitudes and velocities of potentially hidden solitonic components. Under the KdV equation, the nonlinear spectrum evolves trivially according to simple analytic rules. This in particular reflects that solitons are conserved by the KdV equation. However, in reality, the nonlinear spectrum will change during evolution due to deviations from the KdV equation. For example, waves in the ocean are typically multi-directional. Furthermore, the water depth may range into the intermediate regime, e.g. depending on tides and peak periods. It is therefore uncertain how long the nonlinear spectrum of real-world data remains representative. In particular, it is unclear how stable the detected soliton components are during evolution. To assess the effectiveness of the KdV-NFT in representing water wave dynamics under non-ideal conditions, we generated numerical sea states with varying directional spreading in intermediate water ($kh = 1.036$) using the High-Order Spectral Ocean (HOS-Ocean) model for nonlinear evolution. After applying the NFT to space series extracted from these evolving directional wave fields, we observe that the KdV-soliton spectra from the NFT are quite stable for cases with small directional spreading. We in particular observe that the largest soliton amplitude is (sometimes dramatically) more stable than the amplitude of the largest linear mode. For large directional spreading, the applicability is limited to short propagation times and distances, respectively.

1. Introduction

Solitons have been recognized as fundamental building blocks in the field of nonlinear dynamics. Their initial discovery dates back to the experiments by John Scott Russell in 1844 [1]. They were subsequently described mathematically by the Korteweg–De Vries (KdV) equation [2]. The KdV equation provides a mathematical framework for the evolution of weakly nonlinear and dispersive progressive unidirectional free-surface waves in shallow water with a constant water depth.

* Corresponding author.
E-mail address: Y.C.Lee-2@tudelft.nl (Y.-C. Lee).

https://doi.org/10.1016/j.wavemoti.2025.103542
Received 9 September 2024; Received in revised form 20 December 2024; Accepted 11 March 2025
Available online 19 March 2025

The Nonlinear Fourier Transform (NFT)[1] is as a powerful mathematical tool capable of effectively solving the KdV equation [3]. By employing the NFT, we obtain a nonlinear spectrum that reveals physically meaningful nonlinear components with respect to the KdV equation. The solitonic part of the nonlinear spectrum provides amplitudes, velocities, and phases of solitons, offering essential information for understanding the behavior of systems affected by (potentially hidden) solitons. The nonlinear spectrum evolves trivially when the wave propagation is governed by the KdV equation. As there are also NFTs for other (so-called integrable) equations than the KdV, we refer to the KdV-NFT. The KdV-NFT can be used as a signal processing tool [4], and has been utilized to analyze both experimental [5–9] and field measurements [10–14]. Especially in field measurements, the KdV equation can only be an approximate model for wave propagation. In [13], where the measurement site was not specifically chosen to demonstrate the KdV-NFT, non-negligible directional spreading was present and some of the data ventured into intermediate water depths. At the moment, it is not clear what the lifetime of the detected soliton components is. The goal of this paper is to shed some light into this question.

Recently, the paper [15] has explored the impact of directional spreading on the nonlinear Fourier spectrum with respect to the nonlinear Schrödinger equation, which applies to the deep water case. However, there currently is no study that investigates the distance for which KdV solitons can maintain stability during non-ideal evolution. In this paper, we therefore investigate the effects of directional spreading on the solitonic part of KdV-NFT spectra in intermediate water using numerical simulations, and estimate the propagation distances of the soliton components in various scenarios.

To perform the simulations, we utilize a nonlinear phase-resolving wave model based on the High-Order Spectral (HOS) method in order to generate the spatio-temporal evolution of surface wave elevation. We employ the open-source model HOS-Ocean by Ducrozet et al. [16]. HOS-Ocean is based on the Zakharov equation [17], which describes the dynamics of weakly nonlinear and dispersive surface gravity waves in arbitrary constant depths (see the HOS-Ocean repository on GitLab https://gitlab.com/lheea/HOS-Ocean). The HOS-Ocean model has been employed in numerous investigations focused on extreme wave phenomena and rogue waves [18–23]. Simulating nonlinear waves numerically poses a challenge due to the issue of wave breaking [24]. The applicability of the HOS-Ocean model is constrained to non-breaking waves propagating within a uniform water depth. Therefore, wave-breaking conditions should be avoided as discussed in [25,26]. (More details on this aspect are provided in subsequent sections.)

Our paper reports the first results on the impact of directionality on the NFT based on the (uni-directional) KdV equation. The structure of this paper is as follows. The theoretical background of the methods is introduced in Section 2. The simulation set-up is presented in Section 3. The results are presented in Section 4. In Section 4.1, we first show fundamental statistical results for the HOS-Ocean simulation. These results will be used to make a comparison with the KdV evolution under unidirectional conditions in Section 4.2. In Section 4.3, we present the results of the NFT applied to wave fields from the HOS-Ocean model. Two evaluation indices will be used to assess the impact of directional spreading on the evolution of the soliton spectrum in Section 4.4. Finally, we discuss the results and provide a summary in Section 5.

2. Methods

2.1. The high-order spectral method

Simulations of the random surface waves were performed using the open-source model HOS-Ocean [16]. It is based on the High-Order spectral (HOS) method first proposed by [27,28]. HOS-Ocean demonstrates superior efficiency and accuracy in wave propagation when compared to other advanced methods [18,29,30]. It has been widely used to investigate the simulation of rogue waves [18,19,31,32], wave-structure interaction [33], and the effects of ship motion [34].

The model is based on the potential flow formalism, assuming an incompressible, inviscid fluid, and irrotational flow. The Laplace equation for the velocity potential ϕ is solved with boundary conditions. The Laplace equation can be written as

$$\nabla^2\phi + \frac{\partial^2\phi}{\partial z^2} = 0, \tag{1}$$

where ∇ is the gradient operator. The kinematic and dynamic free surface boundary conditions, involving the free surface elevation η and the free surface velocity potential $\widetilde{\phi}(x,t) = \phi(x, z = \eta(x,t), t)$, satisfy

$$\begin{aligned} \frac{\partial\eta}{\partial t} &= \left(1 + |\nabla\eta|^2\right) W - \nabla\widetilde{\phi}\cdot\nabla\eta, \\ \frac{\partial\widetilde{\phi}}{\partial t} &= -g\eta - \frac{1}{2}|\nabla\widetilde{\phi}|^2 + \frac{1}{2}\left(1 + |\nabla\eta|^2\right) W^2, \end{aligned} \tag{2}$$

where W is the vertical velocity at the free surface elevation. It solves the fully nonlinear boundary value problem for two unknowns which are the surface elevation η and velocity potential $\widetilde{\phi}$. HOS-Ocean considers periodic boundary conditions:

$$(\eta, \widetilde{\phi}, W)(x = 0, t) = (\eta, \widetilde{\phi}, W)\left(x = L_x, t\right). \tag{3}$$

The HOS-Ocean model evaluates the vertical velocity W with the HOS nonlinear order M,

$$\phi(x,z,t) = \sum_{m=1}^{M} \phi^{(m)}(x,z,t), \tag{4}$$

[1] The NFT is also known as the forward transform of the inverse scattering method.

where $\phi^{(m)}(x,z,t)$ is assumed to be of order $O(\epsilon^m)$, and ϵ is a measure of the wave steepness. The HOS nonlinear order M enables considering up to $M+1$ nonlinear wave interactions. The nonlinear order M = 2 thus considers the three-wave nonlinear process, while M = 3 considers the four-wave quasi-resonant interactions.

From the mean water level of $z=0$, the velocity potential ϕ can be expanded to other water levels using Taylor series:

$$\begin{aligned}\phi^{(1)}(x,0,t) &= \widetilde{\phi}(x,t),\\ \phi^{(m)}(x,0,t) &= -\sum_{k=1}^{m-1}\frac{\eta^k}{k!}\frac{\partial^k\phi^{(m-k)}}{\partial z^k}(x,0,t) \quad \text{for } m>1.\end{aligned} \tag{5}$$

Once the individual orders of velocity potential $\phi^{(m)}$ are obtained, the vertical velocity W can also be calculated using the Taylor expansion:

$$\begin{aligned}W(x,t) &= \sum_{m=1}^{M} W^{(m)}(x,z,t),\\ W^{(m)}(x,t) &= \sum_{k=0}^{m-1}\frac{\eta^k}{k!}\frac{\partial^{k+1}\phi^{(m-k)}}{\partial z^{k+1}}(x,0,t).\end{aligned} \tag{6}$$

The HOS-Ocean model utilizes a pseudo-spectral method in order to achieve a balance between the high accuracy of spectral methods and the computational efficiency of real-space calculations [16]. This methodology involves representing the solution using a series of basis functions, typically Fourier series, enabling the application of Fast Fourier Transforms (FFTs) for efficient conversion between real and spectral domains. In terms of temporal evolution, HOS-Ocean model commonly employs an efficient 4th order Runge–Kutta Cash-Karp scheme renowned for their precision and stability in integrating equations over time [35]. These methods iteratively propagate the solution forward by computing intermediate steps within each time increment.

2.2. Nonlinear Fourier analysis

Nonlinear Fourier transforms (NFTs) enable the characterization of nonlinear wave dynamics by decomposing waveforms into nonlinearly interacting solitons and radiation waves. This study investigates to which degree the soliton spectrum remains invariant under the evolution of directional free surface waves in intermediate waters, by applying the KdV-NFT to data generated by the HOS-Ocean model.

The spatial KdV equation is

$$u_t + c_0 u_x + \alpha u u_x + \beta u_{xxx} = 0, \tag{7}$$

where $u = u(x,t)$ is the elevation of the free surface elevation at location x and time t, the subscripts donate partial derivatives, $c_0 = \sqrt{g h_0}$ is the linear phase speed in shallow water, g is the gravitational acceleration, h_0 the water depth, $\alpha = 3c_0/2h_0$ is the coefficient of the nonlinearity, $\beta = c_0 h_0^2/6$ is the coefficient of the dispersive term. The KdV equation is derived, as already mentioned earlier, under several assumptions: shallow water, unidirectionality, weak nonlinearity, and a flat bottom. In particular the first two assumptions are often violated for real-world measurements. While shallow water is commonly defined by $kh < \pi/10$, this is not a sharp cut-off. The KdV equation can be used with larger kh, at the price of decreased accuracy. In the literature, various cut-off criteria for the applicability of the KdV equation have been used: $kh \le 1$ [5], $kh \le 1.36$ [36], and $kh \le 1.14$ [11]. These criteria exceed the usual range of shallow water ($kh < \pi/10$) and extend into the intermediate water range ($\pi/10 < kh < \pi$). Figure 1b in [36] illustrates that $kh = 1.14$ corresponds to a 6% mismatch between the shallow water dispersion relation and the dispersion relation of the KdV equation, while $kh = 1.36$ corresponds to a mismatch of 14%. When the threshold kh exceeds 1.363, the modulational instability arises [37,38], causing the underlying wave dynamics to be better described by the nonlinear Schrödinger equation.

We now consider the nonlinear Fourier transform with periodic boundary conditions. There is also a mathematically simpler variant for wave packets [3], but since the data generated by HOS-Ocean is truly periodic, we use the more complicated periodic NFT. In this way, we avoid glitches in the spectrum due to boundary mismatches that would make it harder to isolate the effects we are actually interested in. (For the same reason, we will consider space series instead of time series, as the time series created by HOS-Ocean are not periodic. In lab experiments, it was observed that the solitons detected from space series match those detected from time series very well [8].) The periodic KdV-NFT is defined for so-called finite genus solutions of the KdV equation. Finite genus solutions are linear superpositions of finitely many hyperelliptic functions $\mu_i(x,t)$, representing nonlinearly interacting nonlinear waves [4,5,39]:

$$\lambda u(x,t) = -E_1 + \sum_{i=1}^{N}\left[2\mu_i(x,t) - E_{2i} - E_{2i+1}\right], \tag{8}$$

where $\lambda = \alpha/(6\beta)$ and α and β are physical constants given in the spacial KdV equation. It is known that finite genus solutions can approximate arbitrary periodic solutions. For small-amplitude surface elevations, they turn into Fourier series. The NFT of a finite genus solution consists of several parts, of which will only need the constants E_i. These constitute the so-called main spectrum. For the computation of the main spectrum from a given spatial measurement $u_0(x)$, the second-order Schrödinger eigenvalue problem has to be solved. The Schrödinger eigenvalue problem is given by [4]

$$\psi_{xx} + [\lambda u(x,0) + k^2]\psi = 0, \quad \psi = \psi(x;k^2), \tag{9}$$

where k is the "nonlinear frequency" with $k^2 = E$. The monodromy matrix $\mathbf{M}(k^2)$ is a matrix-valued solution of (9), which is obtained by using the 2×2 identity matrix as an initial condition at an arbitrary point, and propagating it over one period of the waveform. The trace $\Delta(E)$ of the monodromy matrix $\mathbf{M}$ is the Floquet discriminant $\Delta(E) = \frac{1}{2}Tr\mathbf{M}$. The Floquet discriminant shows for which k^2 in Eq. (8) has quasi-periodic solutions [36,40]. The main spectrum can be calculated by finding the solutions of $\Delta(E) = \pm 1$. The constants E_i in the main spectrum correspond to the k^2 for which (9) has periodic (if $\Delta(E) = +1$) and anti-periodic (-1) solutions ψ. Two adjacent eigenvalues determine an open band E_{2i}, E_{2i+1} when $|\Delta(E)| > 1$ for $E_{2i} < E < E_{2i+1}$. There is also an auxiliary spectrum (not shown), which consists of initial conditions $\mu_i(x_0, t_0)$ for the hyperelliptic modes. The nonlinear KdV spectrum is commonly decomposed into soliton and radiation components. The modulus m of the hyperelliptic functions is employed to distinguish between soliton and radiation waves:

$$m_i = \frac{E_{2i+1} - E_{2i}}{E_{2i+1} - E_{2i-1}}, \quad 0 < m_i < 1. \tag{10}$$

A modulus $m_i < 0.99$ indicates an oscillatory mode. For $m_i \geq 0.99$, we have solitons. The amplitude a_i of an hyperelliptic oscillation mode can be expressed as

$$a_i = \frac{E_{2i+1} - E_{2i}}{2\lambda}. \tag{11}$$

The soliton amplitudes η_n are given by

$$A_i = \frac{2(E_{\text{ref}} - E_{2n})}{\lambda}, \quad 1 \leq n \leq N_{\text{sol}}. \tag{12}$$

Here, the number of solitons N_{sol} is the largest N such that $m_i \geq 0.99$ for all $i = 1, 2, \ldots, N$. The reference level $E_{\text{ref}} = E_{2N_{\text{sol}}+1}$ corresponds to the level at which the solitons travel in periodic theory [4,5,41].

To illustrate the periodic KdV-NFT, we now show one example from the HOS-Ocean model. Using basic settings of $H_s = 6$ m, $T_p = 10$ s and $\Theta = 0$, a unidirectional wave field is generated. The space series extracted from the middle of the wave field with respect to the y-direction is shown in Fig. 1(a). After applying the NFT on the space series, the associated Floquet spectrum shown in Fig. 1(b) is found. It consists of the Floquet discriminant $\Delta(E)$ (blue line), main spectrum points (red dots), reference level E_{ref} (pink line) and open bands (red lines). The main spectrum points are located at the intersections of $\Delta(E)$ with ± 1. The reference level is used to distinguish between the soliton components and the radiation components. Solitons are calculated by the Floquet discriminant to the left of reference level, while radiation waves are to the right of reference level. An open band refers to intervals of E (as illustrated in Fig. 15.1 and 17.3–17.5 in Osborne's book [4]). In Fig. 1(c), the hyperelliptic modes are described by their amplitude (blue line) and modulus (red line). One soliton can be found in spectrum with modulus larger than 0.99. The other components are oscillatory waves. A feature of the nonlinear Fourier spectrum is that it can be represented by the linear superposition of cnoidal waves and their interactions with each other [42]. Note that the calculated wave number of the soliton is negative by convention, to separate it from the oscillatory part. For a detailed interpretation of the nonlinear Fourier spectrum obtained from the periodic NFTs based on the KdV equation, see [4,6].

For this paper, the main spectrum part of the periodic KdV-NFT (i.e., the E_i) was computed using a development version of the open source software library FNFT (commit `7bd10db`) [43], which has already been applied to various problem in the context of optical fiber [44–46] and hydrodynamics [13,47–49]. More information about FNFT can be obtained online at https://github.com/FastNFT/FNFT. The moduli, reference level and soliton amplitudes were computed from the main spectrum in a custom Matlab function, which implemented the formulas given above.

3. Simulation setup

The HOS-Ocean model utilizes a directional spectrum of the form $S(\omega, \theta) = F(\omega)G(\theta)$, where $F(\omega)$ is a JONSWAP spectrum and $G(\theta)$ is a directional spreading function. The JONSWAP spectrum is a widely recognized empirical model extensively used for characterizing irregular waves [16]. It takes into account the significant wave height (H_s), angular peak frequency (ω_p), peak enhancement factor (γ), and angular spreading parameter (α):

$$F(\omega) = \alpha_J H_s^2 \omega_p^4 \omega^{-5} \exp\left[-\frac{5}{4}\left(\frac{\omega}{\omega_p}\right)^{-4}\right] \gamma^{\exp\left(-\frac{(\omega-\omega_p)^2}{2\sigma^2\omega_p^2}\right)} \tag{13}$$

with $\sigma = \begin{cases} 0.07 & \text{for} \quad \omega < \omega_p \\ 0.09 & \text{for} \quad \omega \geq \omega_p \end{cases}$, where α_J is a constant to obtain the correct significant wave height. The directional spreading function $G(\theta)$ is defined as [16,50,51]

$$G(\theta) = \frac{1}{\beta}\left[\cos\left(\frac{\pi\theta}{2\beta}\right)\right]^2, \quad \left|\frac{\pi\theta}{2\beta}\right| \leq \frac{\pi}{2}, \tag{14}$$

where β is a measure of the directional spreading. We introduce $\Theta = 2\beta$ in degrees, which represents the range of the directional distribution. The parameter β is suggested to be in the range [0, 0.6], where $\beta = 0.6$ represents a short-crested sea state with very large spreading [25]. In this study, we set the parameter β to 0, 0.0872, 0.1309, 0.1745, 0.2618, 0.5236, which corresponds to $\Theta = 0°$, 10°, 15°, 20°, 30°, and 60°, respectively. Fig. 2(a) depicts the corresponding spreading functions.

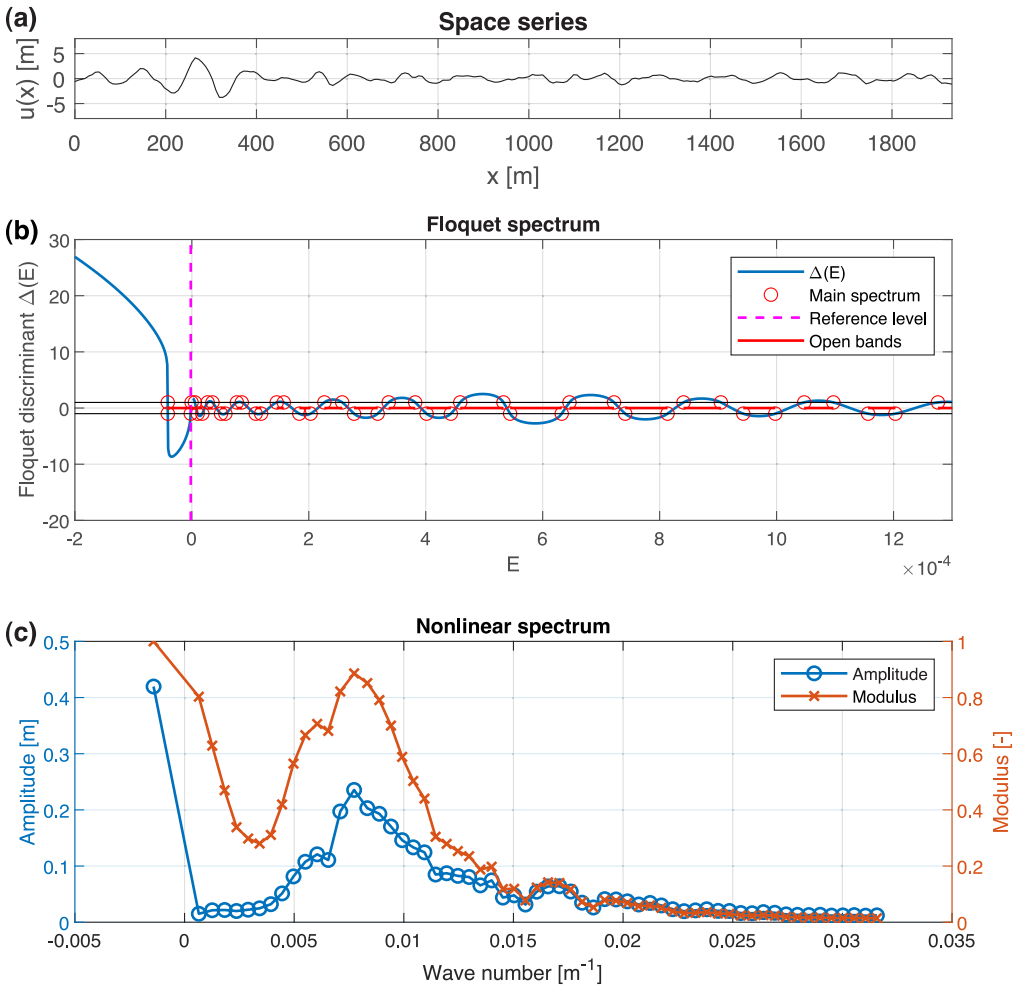

Fig. 1. (a) Example of simulated space series (b) The Floquet spectrum of simulated space series contains the Floquet discriminant $\Delta(E)$ (blue line), main spectrum points (red dots), reference level E_{ref} (pink line) and open bands (red lines). (c) The nonlinear Fourier spectrum of simulated space series. The nonlinear modes are represented by amplitudes (blue circle line) and modulus (red cross line). (For interpretation of the references to color in this figure legend, the reader is referred to the web version of this article.)

The HOS-Ocean model is unable to explicitly describe wave breaking. Guidelines for ensuring the applicability of the model for directional irregular sea states with different water depths have been developed in [25]. In this study, we consider a water depth of 20 m. The threshold for wave breaking in different water depths is, based on the Ref. [52], given by

$$H_b = \kappa \lambda_p \tanh(K_p h), \tag{15}$$

where H_b is the breaking wave height, κ is a coefficient, λ_p is the wave length based on the peak period, k_p is the peak wave number, and h is the water depth. The value of κ varies across locations, depending on the local water depth and environments [53–55]. We use $\kappa \in [0.067; 0.076]$, which is considered suitable for the HOS-ocean model according to [25]. Fig. 2(b) shows the applicability range for the highest possible irregular wave field at different water depths. Under consideration of the non-breaking wave conditions, the wave fields are generated with significant wave heights of $H_s = 4, 5, 6$ m and a peak period of $T_p = 10$ s. The relative water depth kh is equal to 1.036 in our case, which corresponds to an intermediate water depth ($0.1\pi < kh < \pi$) [56,57]. It is nevertheless below the two KdV applicability thresholds discussed earlier, $kh < 1.14$ [11] and $kh < 1.36$ [36].

In this study, we have simulated the evolution of in total 36 wave fields corresponding to different input conditions, as shown in Table 1. We adopted a spatial discretization of $N_x = 256$ and $N_y = 64$ grid points for all simulations, with computational domain lengths of $L_x = 16\lambda_p \simeq 1932.21$ m and $L_y = 8\lambda_p \simeq 954.74$ m, where $\lambda_p = 2\pi/k_p$ is the peak wavelength. The mesh resolution is $\Delta x = L_x/(N_x - 1) \simeq 7.58$ m and $\Delta y = L_y/(N_y - 1) \simeq 15.15$ m. The nonlinear order M is either $M = 2$ or $M = 3$. We point out that all simulations have been carried out at least once including third-order nonlinearities (M = 3). Furthermore, several simulations have been additionally been carried out using only second-order nonlinearities (M = 2). The motivation was to study the impact of third-order nonlinearities in our scenario. (We are considering an intermediate water depth, and it is known that the effects of

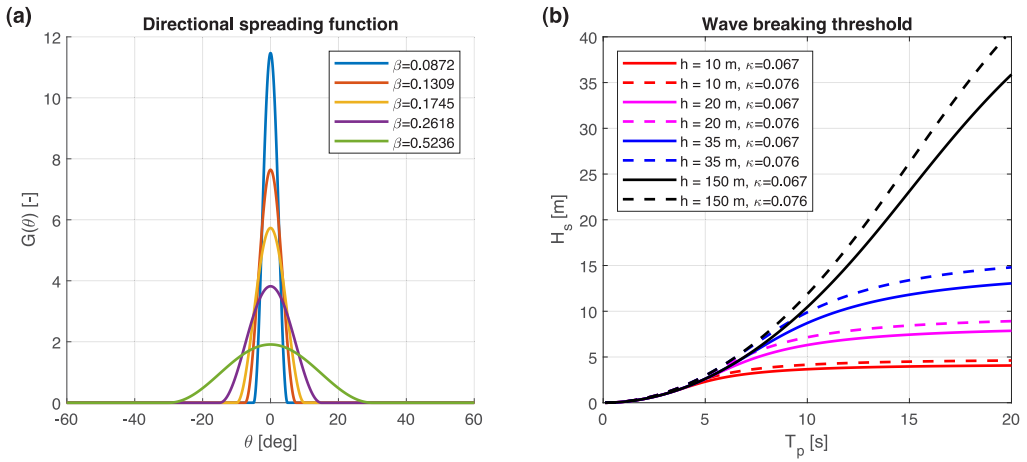

Fig. 2. (a) Directional spreading function $G(\theta)$ of angle θ for different directional spreadings. (b) Applicability limits for HOS simulation with water depths of $h = 10$ m (red lines), $h = 20$ m (purple lines), $h = 35$ m (blue lines) and $h = 150$ m (black lines) with coefficient κ varying from local sites. (For interpretation of the references to color in this figure legend, the reader is referred to the web version of this article.)

Table 1
Input wave parameters of directional seas for the HOS-Ocean simulation.

Case	H_s [m]	T_p [s]	Θ [°]	M	Case	H_s [m]	T_p [s]	Θ [°]	M
1	4.0	10.0	0°	2	19	4.0	10.0	0°	3
2	5.0	10.0	0°	2	20	5.0	10.0	0°	3
3	6.0	10.0	0°	2	21	6.0	10.0	0°	3
4	4.0	10.0	10°	2	22	4.0	10.0	10°	3
5	5.0	10.0	10°	2	23	5.0	10.0	10°	3
6	6.0	10.0	10°	2	24	6.0	10.0	10°	3
7	4.0	10.0	15°	2	25	4.0	10.0	15°	3
8	5.0	10.0	15°	2	26	5.0	10.0	15°	3
9	6.0	10.0	15°	2	27	6.0	10.0	15°	3
10	4.0	10.0	20°	2	28	4.0	10.0	20°	3
11	5.0	10.0	20°	2	29	5.0	10.0	20°	3
12	6.0	10.0	20°	2	30	6.0	10.0	20°	3
13	4.0	10.0	30°	2	31	4.0	10.0	30°	3
14	5.0	10.0	30°	2	32	5.0	10.0	30°	3
15	6.0	10.0	30°	2	33	6.0	10.0	30°	3
16	4.0	10.0	60°	2	34	4.0	10.0	60°	3
17	5.0	10.0	60°	2	35	5.0	10.0	60°	3
18	6.0	10.0	60°	2	36	6.0	10.0	60°	3

third-order nonlinearity reduce close to shallow water conditions [58].) The input parameters for the JONSWAP spectrum are set to $H_s = 4, 5, 6$ m, $T_p = 10$ s and $\gamma = 3.3$. The random phases were fixed by using the same initial seed for the random number generator. The wave fields are evolved for 1200 s. We show an example of nonlinear wave fields at $t = 201$ s with the settings $H_s = 4$ m, $T_p = 10$ s and M = 3 with $\Theta = 0°, 10°, 15°, 20°, 30°, 60°$ in Fig. 3. It should be noted that in HOS-Ocean simulation, the initial wave field is generated using linear solutions. An adjustment period is necessary to manage the transition from linear initial conditions to a nonlinear surface wave field [59,60]. The adjustment duration is recommended for the first 20 wave periods, which in our cases, with a peak wave period of $T_p = 10$ s, amounts to 200 s.

In Fig. 4, we present the spectral evolution of the two-dimensional linear spectrum for a directional spreading of 60° (initial wave field in Fig. 3(f)). The proper wavenumber-domain bandwidth ensures accurate representation of the wave field and efficient numerical computation. The wavenumbers are distributed in the range between $k_{\min}$ and $k_{\max}$. As suggested in [25,61], we select $k_{\max} = 8k_p$ with the peak wave number $k_p = 2\pi/\lambda_p$ as the bandwidth of the reconstructed wave field.

4. Results

Utilizing the HOS-Ocean model with the aforementioned settings, we discuss the nonlinear spectral characteristics of the wave field under different directional spreading. We first present conventional statistical results for the simulated wave fields in Section 4.1 to characterize the simulation setup, and contrast these results with a KdV-based evolution in Section 4.2. The temporal evolution of the nonlinear KdV-type soliton spectrum under the HOS model is presented in Section 4.3 to assess the impact of directional spreading and intermediate water conditions. In Section 4.4, we then quantify the impact of directional spreading on the KdV-NFT soliton spectra. Finally, in Section 4.5, the evolution of the largest soliton is compared to that of the largest linear mode.

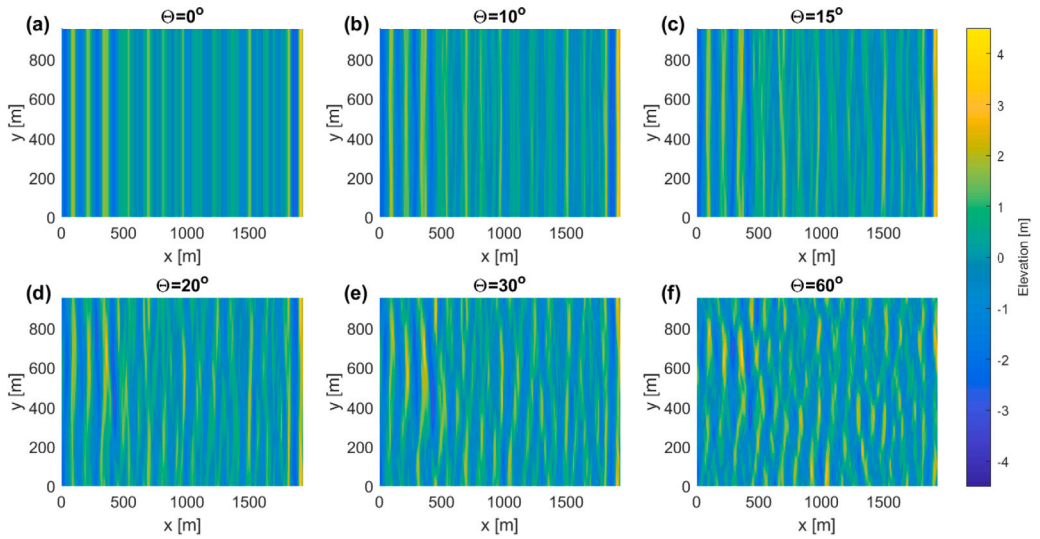

Fig. 3. Simulated wave fields by HOS-Ocean model with conditions of $H_s = 4$ m and $T_p = 10$ s at $t = 201$ s by HOS-Ocean model under different directional spreading conditions: (a) $\Theta = 0°$ (b) $\Theta = 10°$ (c) $\Theta = 15°$ (d) $\Theta = 20°$ (e) $\Theta = 30°$ (f) $\Theta = 60°$.

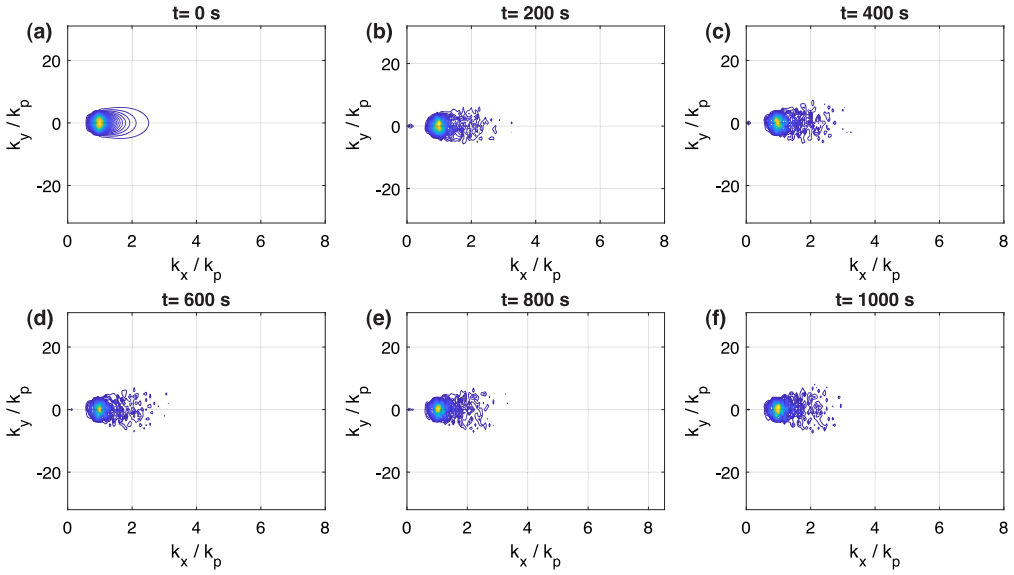

Fig. 4. Evolution of wave spectrum with $H_s = 4$ m, $T_p = 10$ s, and $\Theta = 30°$ by the HOS-Ocean model during nonlinear propagation at (a) $t = 0$ s (b) $t = 200$ s (c) $t = 400$ s (d) $t = 600$ s (e) $t = 800$ s (f) $t = 1000$ s.

4.1. Statistical characteristics during nonlinear evolution

The simulated wave fields correspond to two conditions with nonlinear order M: $M = 2$ and $M = 3$. Three parameters including maximum wave height, kurtosis, and skewness are used to represent spectral characteristics. Kurtosis measures wave height concentration around the mean, with high values indicating intense, steep waves and low values suggesting uniform distribution [62,63]. Skewness assesses distribution asymmetry, with positive values implying a prevalence of taller, sharper crests and shallower, more rounded troughs [62]. The skewness and kurtosis can be expressed as

$$\text{Skewness} = \frac{\overline{\eta^3}}{\sigma^3}, \tag{16}$$

$$\text{Kurtosis} = \frac{\overline{\eta^4}}{\sigma^4}, \tag{17}$$

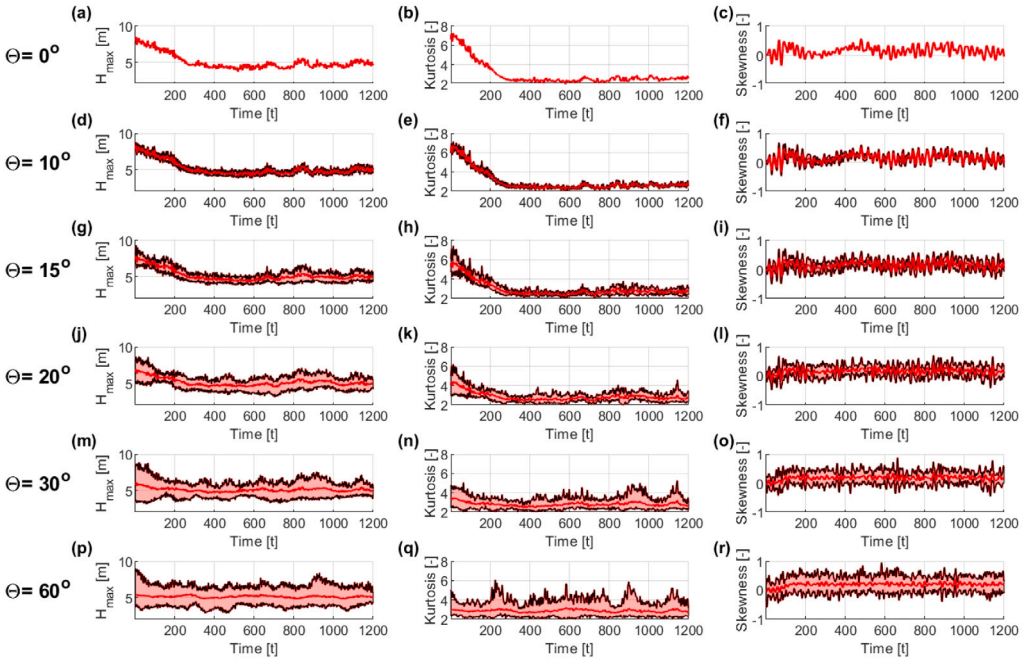

Fig. 5. Statistical results of maximum wave height, kurtosis and skewness of wave fields with $H_s = 4$ m, $T_p = 10$ s, and M = 2 under nonlinear wave evolution with different directional spreadings. The results are presented with the maximum shown by the upper black line, the minimum by the lower black line, and the mean by the middle red line. (For interpretation of the references to color in this figure legend, the reader is referred to the web version of this article.)

where σ is the standard deviation of the surface elevation η, and the overbar indicates the time average operator.

In Figs. 5 and 6, we show exemplary statistical results for the wave field with $H_s = 4$ m and $T_p = 10$ s for two conditions, where $M = 2$ and $M = 3$. We first focus on the $M = 2$ case. For directional spreading $\Theta = 0°$ (Fig. 5(a)–(c)), the wave field is long-crested and aligned in the x-direction. As mentioned in Section 3, the first 20 periods represent the transition from linear solutions to nonlinear behavior. The statistical and spectral wave characteristics become stationary after the transition stage. This characteristic can also be observed in both Figs. 5 and 6. The maximum wave height of the initial space series is 8 m. During the transition stage, the maximum wave height decreases and settles at around 5 m afterward. A similar trend can also be observed in the kurtosis, which starts at 6.6, decreases during the transition, and finally stabilizes at around 2.5. The skewness is also unstable during the first 20 periods, thereafter, it mostly maintains values above 0. The maximum value of skewness observed throughout the evolution is 0.53. A normal distribution has a kurtosis of 3, whereas our simulation's kurtosis of 2.5 is slightly lower than that of a normal distribution, indicating that extreme values of wave elevation are slightly less common than in a normal distribution. Additionally, the positive skewness during the evolution suggests a noticeable asymmetry in our simulation.

When directionality is introduced to a long-crested wave field (starting from Fig. 5(d)), it leads to a transition to short-crested waves, which exhibit a more chaotic pattern. The wave energy is distributed spatially across a range of directions based on the directional spreading. The directionality alters the wave pattern along the y-direction. The statistical parameters such as the maximum (upper line), minimum (lower line), and mean (middle line) values are computed across all spatial series in the y-direction. The statistical parameters of the HOS wave fields under different directional spreading with $\Theta = 10°$, 15°, 20°, 30°, and 60° are depicted in Fig. 5(c)–(r). With increasing directional spreading, it is evident that the statistical parameters including maximum wave height, kurtosis, and skewness exhibit a wider variation range from minimum to maximum values. If we compare the maximum wave height under directional spreading with $\Theta = 60°$ (Fig. 5(p)) with the unidirectional case (Fig. 5(a)) after the transition stage ($t > 200$) s, it is observed that as waves are distributed in the y-direction in the multi-directional case, the interaction among waves results in larger waves compared to the unidirectional case. The largest maximum wave height of $H_{\max} = 8.42$ m is detected at $t = 930$ s. Similar results are observed in kurtosis (Fig. 5(q)) and skewness (Fig. 5(r)). The largest kurtosis value is Kurtosis = 6.09 at $t = 225$ s, while the largest skewness value is Skewness = 0.96 at $t = 582$ s.

Subsequently, we compare the nonlinear orders $M = 2$ (Fig. 5) and $M = 3$ (Fig. 6). The overall results are very similar; however, there are more extreme values of the statistical parameters are observed in the $M = 3$ cases. Considering that third-order nonlinearity is typically more pronounced in deep water conditions, and our simulations are conducted under intermediate water conditions, the third-order effects are not as prominent in our cases. Nonetheless, they still contribute slightly to enhancing the statistical parameters. The statistical results here are quite similar to the simulations of two-dimensional shallow water waves using the Kadomtsev–Petviashvili equation by Toffoli et al. (2008) [64], suggesting that the interaction of two crossing wave trains in shallow water may increase skewness and kurtosis under certain crossing angles.

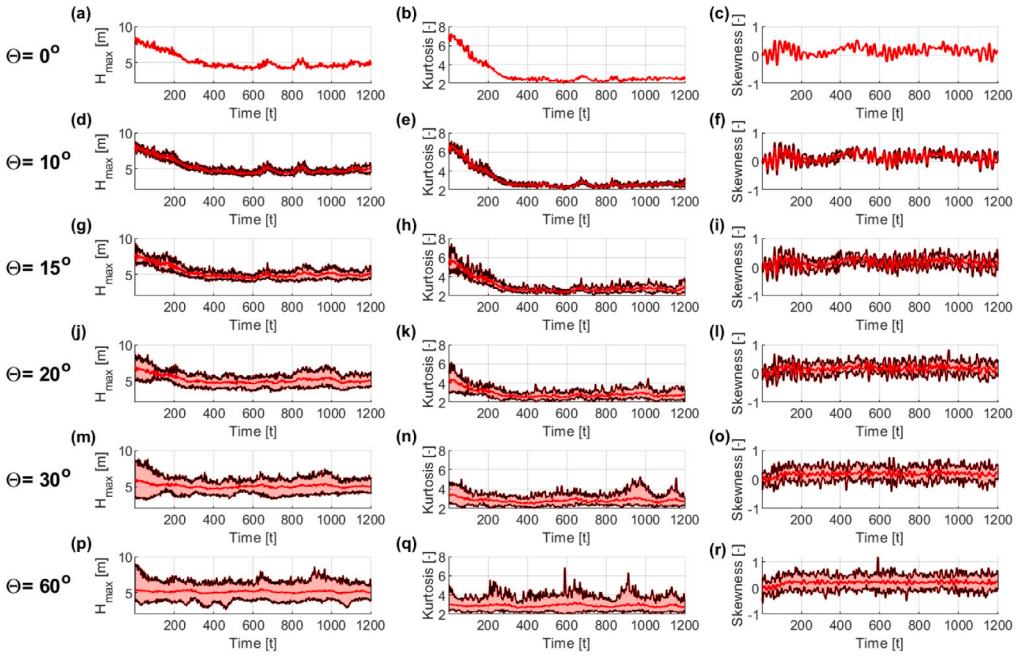

Fig. 6. Statistical results of maximum wave height, kurtosis and skewness of wave fields with $H_s = 4$ m, $T_p = 10$ s, and M = 3 under nonlinear wave evolution with different directional spreadings. The results are presented with the maximum shown by the upper black line, the minimum by the lower black line, and the mean by the middle red line.

4.2. Comparison with spectral characteristics obtained from KdV-dynamics

Similarly to the HOS model considered in the previous subsection, the nonlinear dynamics of random wave fields governed by the KdV equation exhibits different behavior compared to wave evolution by linear wave theory. As nonlinearity increases in the system, the wave fields deviate from a near-Gaussian distribution towards greater asymmetry, characterized by increased kurtosis and positive skewness [65]. This could occur under the interaction of two crossing wave trains in a two-dimensional wave field [64].

In the previous section, we showed the statistical results of the HOS simulation during temporal evolution. The question here is whether the temporal evolution of the HOS wave field under unidirectional conditions resembles that of the KdV equation. The statistical comparison of nonlinear wave fields under unidirectional conditions by the HOS-Ocean model and the KdV equation is illustrated in Fig. 7 for $M = 2$ and 8 for $M = 3$. For applying the HOS-Ocean model, the first 20 periods of the simulation should be neglected to avoid the transition stage as it becomes nonlinear (as mentioned in Section 3). The spatial series at $t = 201$ s is chosen as the initial input for the Korteweg–de Vries (KdV) equation. The temporal evolution will be simulated for 1000 s to compare the statistics of the propagated waveform with the HOS-Ocean model. The temporal evolution using the KdV equation is performed using the `spin` command of the Matlab package Chebfun [66]. The numerical settings for Chebfun include 10,000 grid points and a time step of $dt = 0.1$ s. The propagation time is set as 1000 s with an interval of 1 s, which allows a comparison with the HOS-Ocean simulation. In Fig. 7(a) with the condition of $H_s = 4$ m, it is observed that the maximum wave height $H_{\max}$ of KdV evolution can exceed that of the HOS-Ocean model. Similar results can be found in Fig. 7(d) with $H_s = 5$ m and (g) $H_s = 6$ m. Similar to maximum wave height, kurtosis in the KdV evolution tend to be larger than those obtained from the HOS-Ocean model, as shown in Fig. 7(b,e,h). Regarding skewness, depicted in Fig. 7(c, f, i), the skewness has more positive and larger values in the HOS simulation than in the KdV equation during temporal evolution. This suggests that the HOS-Ocean model generates wave fields with greater asymmetry during evolution, whereas the KdV equation produces more symmetrical wave fields.

Considering the nonlinear order $M = 3$, Fig. 8 depicts the temporal evolution of statistical parameters for the HOS wave field including third-order nonlinearity. We had observed that the evolution of maximum wave heights for the three different conditions with $M = 3$ is slightly larger than the corresponding conditions for $M = 2$. However, the KdV equation evolution does not exhibit this trend of $M = 3$ cases exceeding the corresponding $M = 2$ conditions. (The KdV equation itself is of course not influenced by the nonlinear order parameter M of the HOS model. Only its initial conditions, which are extracted from the HOS model at $t = 201$ s, change.) As shown in Fig. 8(g), the maximum wave height of the HOS-Ocean model can be larger than that of the KdV equation during evolution. Similar results are observed for kurtosis and skewness, where $M = 3$ cases are larger than $M = 2$, but this trend is not observed in the KdV evolution. Our results show that both methods exhibit different nonlinear evolution properties even under unidirectional conditions. This difference can be attributed to two main factors. First, the applicability of the KdV equation is more suitable for shallow water conditions, whereas the wave fields by HOS-ocean are modeled under intermediate water condition in this study. Second, the KdV equation is, in contrast to HOS-Ocean, only a weakly nonlinear model.

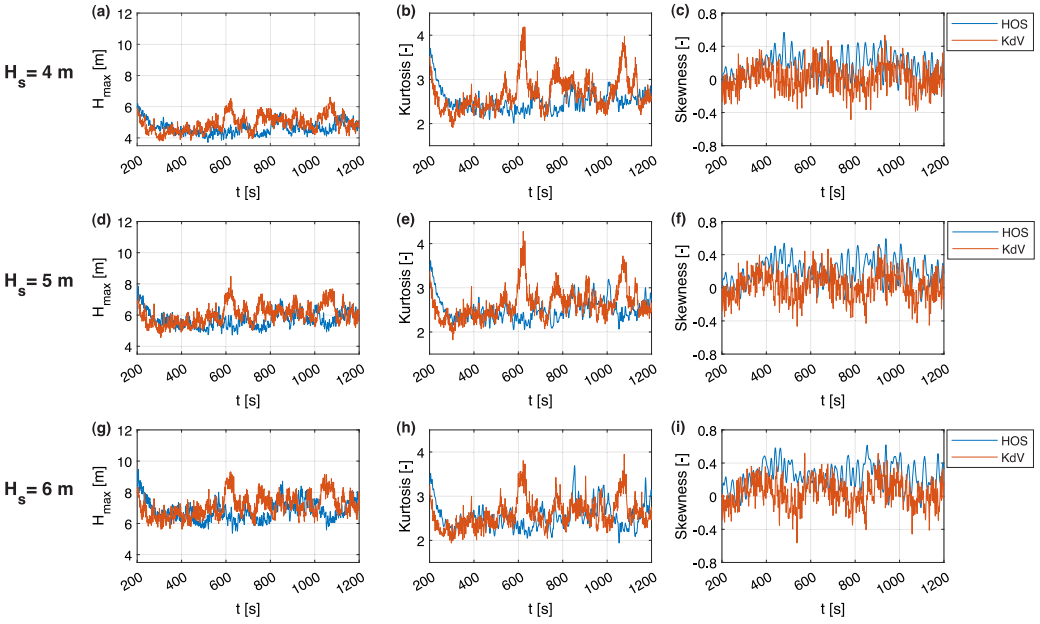

Fig. 7. Comparison of the HOS-Ocean model with the KdV equation under unidirectional conditions. The nonlinear order M = 2 is used. The parameters maximum wave height, kurtosis, and skewness are examined for $H_s = 4$ m, $H_s = 5$ m, and $H_s = 6$ m. The blue line represents the HOS-Ocean model, and the orange line represents the KdV evolution. (For interpretation of the references to color in this figure legend, the reader is referred to the web version of this article.)

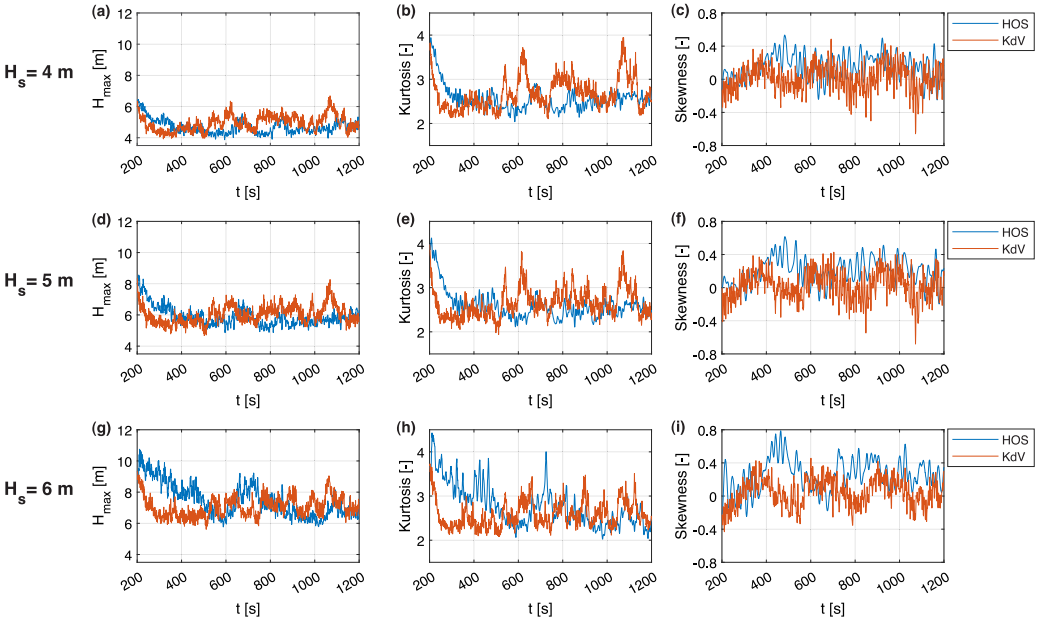

Fig. 8. Comparison of the HOS-Ocean model with the KdV equation under unidirectional conditions. The nonlinear order M = 3 is used. The parameters maximum wave height, kurtosis, and skewness are examined for $H_s = 4$ m, $H_s = 5$ m, and $H_s = 6$ m. The blue line represents the HOS-Ocean model, and the orange line represents the KdV evolution. (For interpretation of the references to color in this figure legend, the reader is referred to the web version of this article.)

4.3. Change of the nonlinear KdV-soliton spectrum under HOS dynamics

In this section, we show the results of the nonlinear Fourier analysis of the wave fields simulated using the HOS-Ocean model. The space series required by the NFT are extracted from the wave fields by considering only the center with respect to the y-direction. By

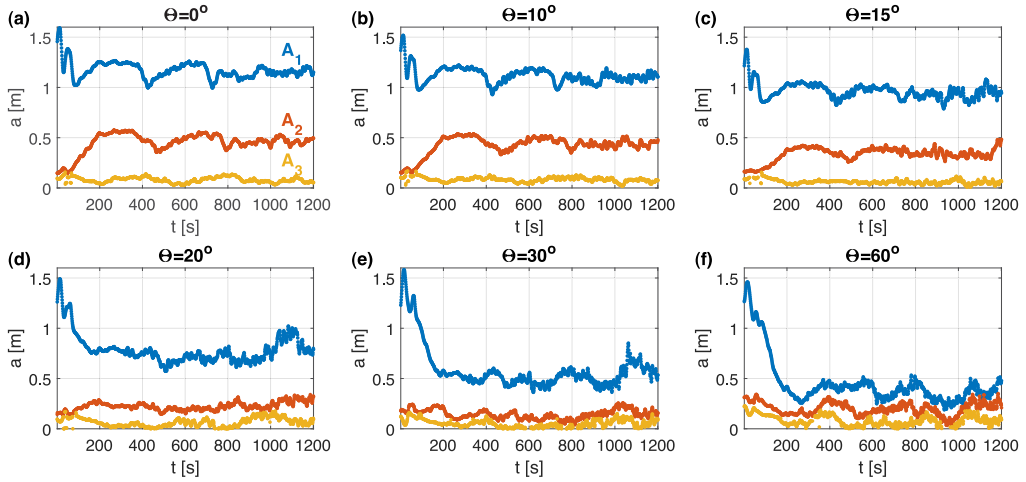

Fig. 9. The amplitudes of solitons in soliton spectra of HOS wave fields with M = 3 under the conditions of significant wave height H_s = 6 m. Different directional spreadings are considered $\Theta = 0°$, $\Theta = 10°$, $\Theta = 15°$, $\Theta = 20°$, $\Theta = 30°$, $\Theta = 60°$ from (a) to (f), respectively. The amplitudes of the largest soliton A_1 is represented by the blue line, second-largest soliton A_2 by the red line, and third-largest soliton A_3 by the yellow line. (For interpretation of the references to color in this figure legend, the reader is referred to the web version of this article.)

applying the NFT with periodic boundary conditions to a specific space series (i.e., for some fixed time $t = t_0$), the nonlinear Fourier spectra are obtained. In our simulations, the modulus of the first amplitude of hyperelliptic oscillation modes, A_1, is consistently greater than 0.99, indicating the presence of a soliton. In the following, we call A_1 the amplitude of the largest soliton. Similarly, when present, A_2 and A_3 denote the amplitudes of the second- and third-largest solitons, respectively.

Recall that soliton amplitudes are calculated using a reference level in the periodic KdV-NFT (12). As mentioned in Section 2.2, the reference level is considered to be the propagation level of solitons. Typically, it differs from the still water level [41]. In practice, it is found by checking when the modulus of the hyperelliptic modes drops below the threshold of 0.99. When applying the NFT to wave fields generated by the HOS-Ocean model, we encountered a critical issue: the soliton amplitudes regularly made implausible large jumps. The discontinuities arise from the use of a fixed threshold. Under non-KdV evolution, the moduli of the hyperelliptic change during propagation. When a modulus passes the threshold, the reference level jumps suddenly due to the way it is computed. To address this issue, we use the maximum reference level seen throughout the temporal evolution as the reference level for each individual space series. With this revision, we obtain soliton amplitudes that change continuously over time.

Based on the above revision of the reference level, we first show that the solution amplitudes evolve continuously in our simulated wave fields with $M = 3$, $H_s = 6$ m, in Fig. 9. In this case, there are in total three soliton components, where the amplitudes of the largest soliton A_1 is represented by the blue line, second-largest soliton A_2 by the red line, and third-largest soliton A_3 by the yellow line. In unidirectional case with $\Theta = 0°$ in Fig. 9(a), we can observe that amplitudes of the three soliton components are quite stable after the transition stage. This feature is also observed in the cases with directional spreading. Even at larger directional spreading ($\Theta = 60°$), A_1 consistently maintains a higher amplitude than A_2. Furthermore, there is no crossover between the amplitudes during temporal evolution, indicating that there is almost no energy exchange among them.

Subsequently, we focus on the amplitude of the largest soliton A_1 as the dominant representative of the soliton spectrum. In Fig. 10, we show how the amplitude of the largest soliton A_1 changes during temporal evolution of HOS-Ocean model with $M = 2$ under various significant wave heights (H_s = 4, 5, and 6 m) and directional spreadings (Θ = 0°, 10°, 15°, 20°, 30°, 60°). In Fig. 10(a), it can be observed that A_1 changes most slowly and remains quite stable under unidirectional spreading. In ideally KdV-governed wave fields, the soliton amplitude would remain constant during evolution. Our results thus show that the non-ideal evolution conditions (from a KdV perspective) in the HOS-ocean simulations only have minor effects on the soliton spectrum under uni-directional spreading. Variations in the amplitudes of the soliton increase with greater directional spreading. According to Fig. 3, we see that wavelengths are quite short compared to the simulated wave fields in the y-direction, and thus wave groups can enter or leave the area where the space series is measured. When considering larger significant wave heights in Fig. 10(b) and (c), the variations of A_1 also increase due to higher nonlinearity in the system, which increasingly deviates from the weakly nonlinear assumption of the KdV equation. Nevertheless, for cases with comparatively small directional spreadings ($\Theta \leq 30°$), the variations of the soliton amplitudes hardly increases. Only for $\Theta = 60°$, a noticeable increase in the variation of A_1 is observed.

Fig. 11 shows the temporal evolution of the amplitude of the largest soliton A_1 in a nonlinear wave field modeled by the HOS-Ocean model with $M = 3$. The temporal evolution of A_1 is quite similar to the case $M = 2$ in Fig. 10, but A_1 in the $M = 3$ case is slightly larger than in the $M = 2$ case. This indicates that the third-order nonlinearity increases the amplitude of A_1, and it is more pronounced in wave fields with larger significant wave height. It also leads to somewhat larger variations of A_1 when the significant wave height is large (H_s = 6 m), compared to the cases with $M = 2$.

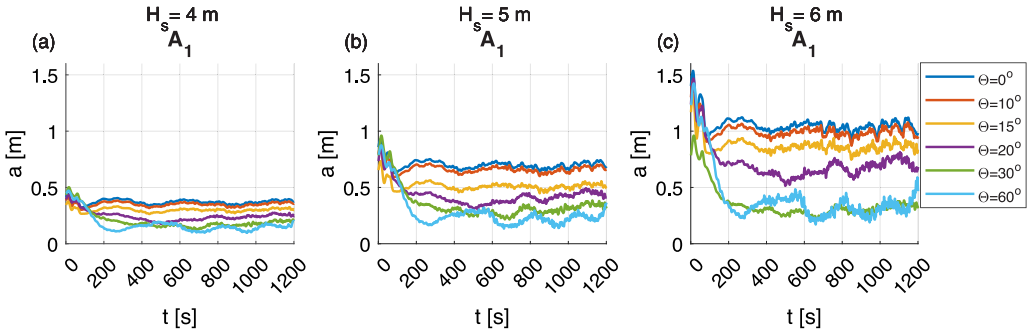

Fig. 10. The amplitudes of the largest soliton A_1 in soliton spectra of HOS wave fields with M = 2 under the conditions of significant wave height (a) $H_s = 4$ m, (b) $H_s = 5$ m and (c) $H_s = 6$ m with directional spreadings $\Theta = 0°$, $\Theta = 10°$, $\Theta = 15°$, $\Theta = 20°$, $\Theta = 30°$, $\Theta = 60°$.

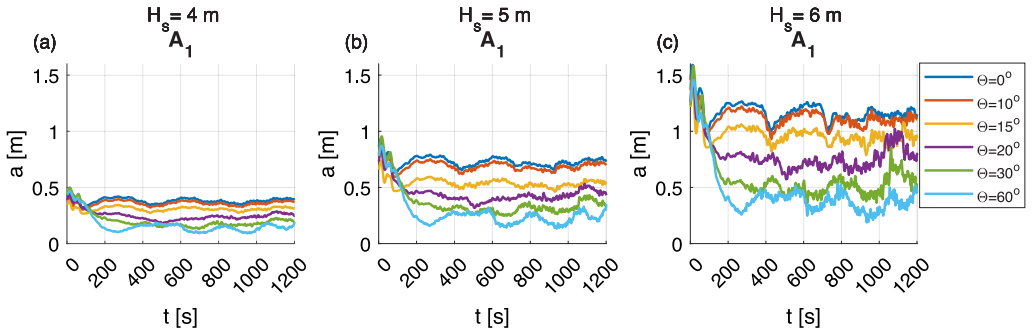

Fig. 11. The amplitudes of the largest soliton A_1 in soliton spectra of HOS wave fields with M = 3 under the conditions of significant wave height (a) $H_s = 4$ m, (b) $H_s = 5$ m and (c) $H_s = 6$ m with directional spreadings $\Theta = 0°$, $\Theta = 10°$, $\Theta = 15°$, $\Theta = 20°$, $\Theta = 30°$, $\Theta = 60°$.

4.4. Quantification of the impact of directional spreading on nonlinear KdV-soliton spectra in intermediate water conditions

We use the largest solitons as representatives of the nonlinear spectrum when describing the nonlinear evolution of shallow water waves. However, in the case of larger directional spreading, part of the soliton's energy may travel into other regions that our selected space series does not capture, causing a larger variation in soliton amplitude. In order to quantify the impact of directional spreading on nonlinear soliton spectra during temporal evolution, we consider the Relative Error (RE) and the Relative Deviation of the Mean (RDM). Denoting the amplitude of largest soliton at time t by $A_1(t)$, the relative error (RE) is the relative change in $A_1(t)$ compared to its value at the end of the HOS-Ocean start-up phase after (i.e., at $t = 201$ s):

$$\mathrm{RE}(t) = \frac{|A_1(t) - A_1(201)|}{A_1(201)}. \tag{18}$$

The second evaluation parameter, Relative Deviation of the Mean (RDM), focuses on the deviation of the average amplitude of the largest soliton over the time interval $[201, t]$ from the initial value:

$$\mathrm{RDM}(t) = \frac{\left| \frac{\sum_{201}^{t} A_1(t)}{t-200} - A_1(201) \right|}{A_1(201)}. \tag{19}$$

Due to the averaging, the RDM results in smoother curves than the RE. We use these two evaluation indices to assess the impact of directional spreading on nonlinear soliton spectra, as shown in Fig. 12 for $M = 2$ and Fig. 13 for $M = 3$.

Fig. 12 shows the temporal evolution of the RE and RDM of the soliton amplitude $A_1(t)$ for shallow water waves fields with $M = 2$ and significant wave heights of (a, d) $H_s = 4$ m, (b, e) $H_s = 5$ m, (c, f) $H_s = 6$ m. We focus on the practically relevant initial stage and observe when the RE and RDM, respectively, hit fixed thresholds for the first time. (Under ideal propagation according to the periodic KdV equation, this would never happen as both indicators would stay zero forever.) We use the unidirectional case with $\Theta = 0°$ as a baseline to determine these thresholds. In Fig. 12(a), we first focus on the unidirectional case of $\Theta = 0°$ with $H_s = 4$ m, where the RE reaches a first major maximum of RE = 0.15 after 236 s before, and the RDM reaches a first major maximum of RDM = 0.065 after 346 s. Under unidirectional conditions, the RE never exceeds 0.15 and the RDM never exceeds 0.071. In the following, we therefore use the more stringent thresholds RE = 0.10 and RDM = 0.05.

We then calculate the propagation times required for the RE to reach 0.1 and the RDM to reach 0.05 for all directional spreadings ($\Theta = 0°$, 10°, 15°, 20°, 30°, 60°). The results show that the durations for these cases are 213 s, 202 s, 178 s, 112 s, 37 s and 16 s,

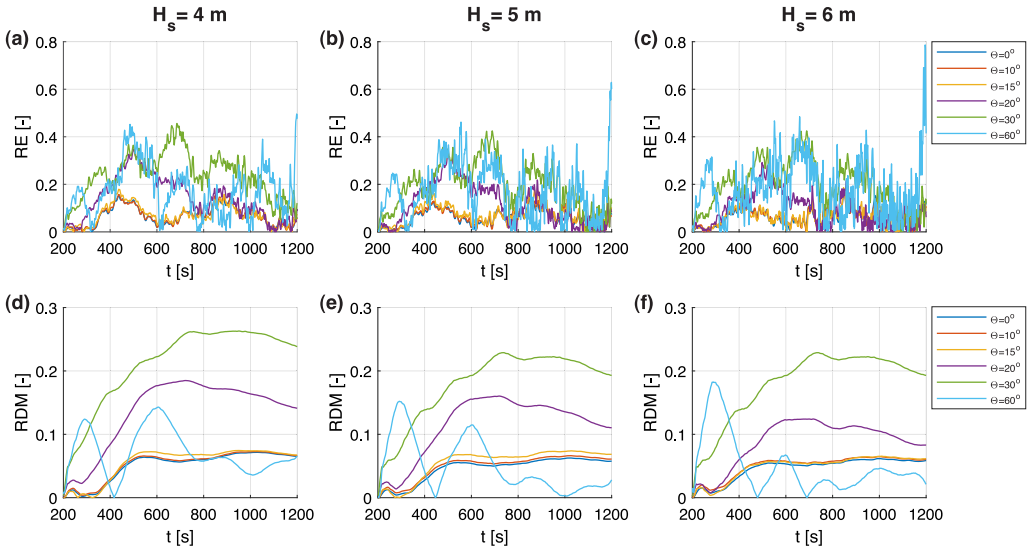

Fig. 12. Evaluation of the amplitude of largest soliton A_1 by relative error (RE) and relative deviation of the mean (RDM) based on the HOS wave fields with M = 2 under the conditions of significant wave heights $H_s = 4$ m, $H_s = 5$ m and $H_s = 6$ m, and directional spreading $\Theta = 0°$, $\Theta = 10°$, $\Theta = 15°$, $\Theta = 20°$, $\Theta = 30°$ and $\Theta = 60°$.

respectively. We also evaluate the propagation time with the RDM shown in Fig. 12(d). When it reaches 0.05, we obtain results of 268 s, 255 s, 246 s, 142 s, 24 s and 22 s for corresponding directional spreadings. The corresponding results for $H_s = 5$ m (see Fig. 12(b,e)) and $H_s = 6$ m (shown in Fig. 12(c,f)) are provided in Table 2. It can be observed that under smaller directional spreading conditions ($\Theta \leq 20°$), the representative propagating time can last more then 110 s. For larger directional spreading conditions ($\Theta \geq 30°$), the RE and RDM deviate significantly faster, resulting in a reduced representative propagation time. This finding is consistent for all significant wave heights.

The evaluation of the impact of directional spreading on the soliton amplitude for $M = 3$ is provided in Fig. 13 and Table 2. In Fig. 13, it can be observed that the RE and RDM with directional spreadings of $\Theta = 0°, 10°$ and $15°$ are almost the same. The RE and RDM start to increase when the directional spreading becomes larger ($\Theta \geq 20°$). The general behavior of the errors in case of $M = 3$ is quite similar to the results for $M = 2$. Based on Table 2, the representative propagation times for $M = 3$ closely resemble the case for $M = 2$.

To estimate a representative propagation distance for solitons, we consider a single solitary wave $u(x,t) = A\mathrm{sech}^2[(x - ct)/l]$, where $c = \sqrt{g(h + A)}$ is the wave celerity and $l = \sqrt{4h^3/(3A)}$ is the characteristic length [4,67,68]. For a wave field with $M = 2$, $H_s = 4$ m and $h = 20$ m, a soliton amplitude of 0.4 m can be read off in Fig. 10(a). The corresponding wave celerity is calculated as 14.15 m/s. For small directional spreading ($\Theta \leq 15°$), propagation times of at least $t_{\mathrm{prop}} = 178$ s can result in propagation distances larger than $c \times t_{\mathrm{prop}} = 14.15\ \mathrm{m/s} \times 178\ \mathrm{s} \approx 2519$ m. Compared to the characteristic length of a soliton with amplitude 0.4 m, which equals 163.3 m, this propagation distance is about 15.4 times the characteristic length. In contrast, with large directional spreading ($\Theta = 60°$), a propagation time of 16 s yields a calculated propagation distance of only around 226 m. In this case, the nonlinear spectrum remains representative for approximately 1.4 times of characteristic lengths. This suggests that the NFT-based method can capture the nonlinear evolution of waves with directional spreading for limited propagation times or distances, which decrease with increasing directional spreading and significant wave height.

4.5. Comparison with linear Fourier modes

To compare our results with the linear Fourier method, we also calculated the RE of the dominant linear Fourier mode during temporal evolution. Based on the HOS wave fields with $M = 3$ and $H_s = 6$ m, we show the results in Fig. 14. The RE of the largest linear Fourier mode obtained by the fast Fourier transform (FFT) and is marked by a blue line. The largest nonlinear mode (soliton) obtained by the NFT is marked with a red line. The RE of the largest linear mode increases faster than the RE of the largest soliton in the practically important initial phase for all cases except $\Theta = 60°$. For the cases with $\Theta \leq 20°$, the soliton RE even stays close to zero for a significant time, while the linear mode RE in contrast increases immediately. These results suggest that the nonlinear Fourier transform may be a more appropriate method for describing the nonlinear evolution of directional wave fields than the conventional linear FFT, even under non-ideal intermediate water and moderate directional spreading conditions.

5. Discussion and conclusions

This paper evaluated the impact of directional spreading and intermediate water conditions on soliton components detected using the nonlinear Fourier transform (NFT) for the Korteweg–de Vries (KdV) equation. Under ideal KdV propagation, the soliton

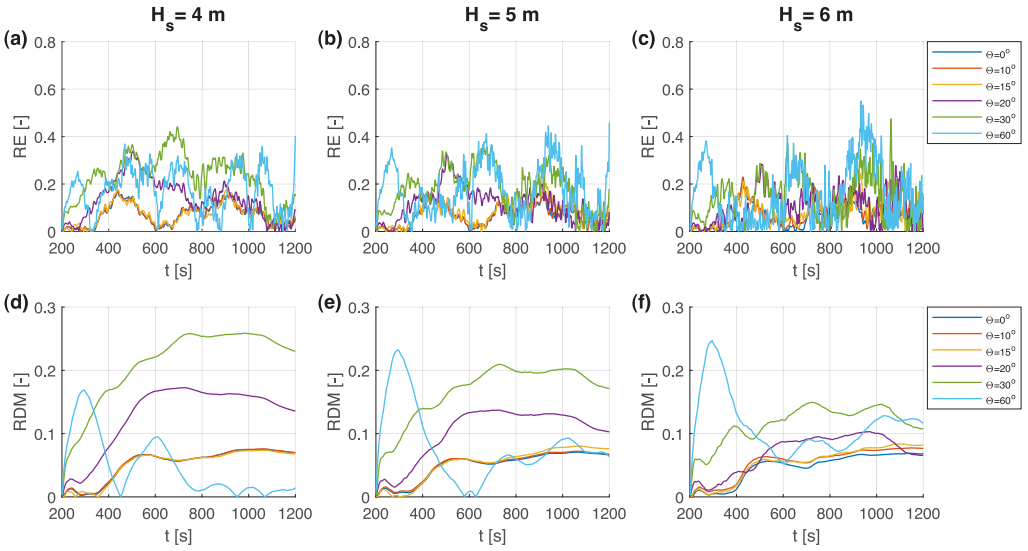

Fig. 13. Evaluation of the amplitude of largest soliton A_1 by relative error (RE) and relative deviation of the mean (RDM) based on the HOS wave fields with M = 3 under the conditions of significant wave heights $H_s = 4$ m, $H_s = 5$ m and $H_s = 6$ m, and directional spreading $\Theta = 0°$, $\Theta = 10°$, $\Theta = 15°$, $\Theta = 20°$, $\Theta = 30°$ and $\Theta = 60°$.

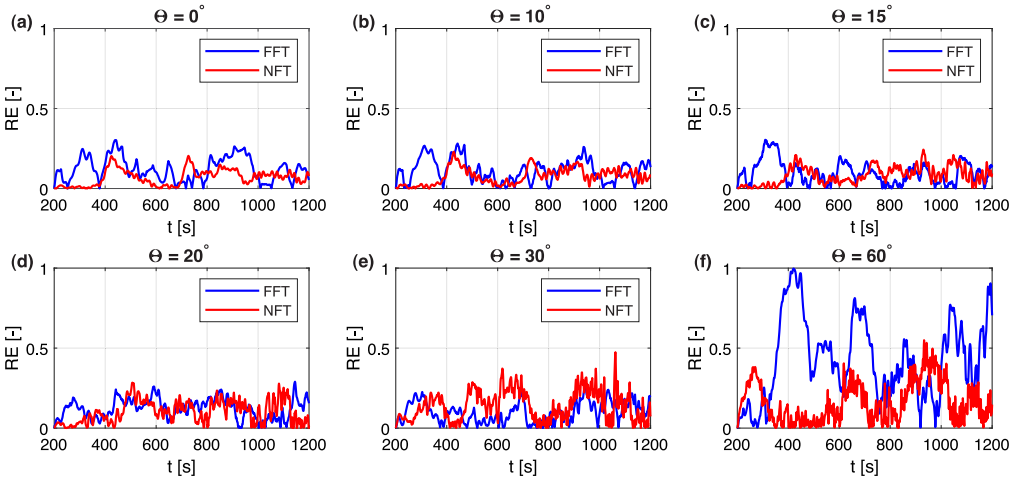

Fig. 14. Evaluation of the amplitudes of dominant linear Fourier modes by relative error (RE) based on the HOS wave fields with M = 3 under the conditions of significant wave heights $H_s = 6$ m, and directional spreading $\Theta = 0°$, $\Theta = 10°$, $\Theta = 15°$, $\Theta = 20°$, $\Theta = 30°$ and $\Theta = 60°$ from (a) to (f), respectively. (For interpretation of the references to color in this figure legend, the reader is referred to the web version of this article.)

amplitudes would stay constant during propagation. Directional spreading and intermediate water conditions however violate the assumptions of the KdV equation, so that the soliton amplitudes are expected to change during propagation. We explored how long the soliton amplitudes remain representative for different directional spreading conditions. To this end, the nonlinear evolution of randomly generated wave fields was simulated using the HOS-Ocean model [16] for various directional spreadings under intermediate water conditions ($kh = 1.036$).

The nonlinear temporal evolution of wave fields was simulated using the HOS-Ocean model for sea states with significant wave heights $H_s = 4$ m, $H_s = 5$ m and $H_s = 6$ m, respectively. A statistical analysis of basic wave parameters during nonlinear evolution was then performed. The evolution of several statistical parameters was compared between the HOS-Ocean model and the KdV equation. This confirmed that the two methods exhibit different nonlinear evolution. Although the KdV equation has limitations in its applicability, we found that the soliton amplitudes obtained from the KdV-NFT nevertheless may vary only slightly during the nonlinear evolution of directional intermediate water waves for certain propagation times or distances, depending on the directional spreading conditions. Moreover, we observed that except for strong spreading conditions, the largest soliton is more stable than the largest linear Fourier mode.

Table 2
Representative propagation time for the nonlinear spectra under different directional spreading conditions.

	M = 2						M = 3					
	$H_s = 4$ m		$H_s = 5$ m		$H_s = 6$ m		$H_s = 4$ m		$H_s = 5$ m		$H_s = 6$ m	
0°	213 s	268 s	215 s	289 s	216 s	247 s	212 s	265 s	201 s	271 s	200 s	281 s
10°	202 s	255 s	216 s	262 s	198 s	243 s	202 s	259 s	202 s	265 s	200 s	249 s
15°	178 s	246 s	161 s	239 s	161 s	241 s	182 s	267 s	184 s	283 s	201 s	266 s
20°	112 s	142 s	131 s	161 s	137 s	180 s	133 s	150 s	135 s	171 s	161 s	289 s
30°	37 s	24 s	75 s	27 s	75 s	27 s	35 s	15 s	77 s	15 s	86 s	15 s
60°	16 s	22 s	14 s	21 s	13 s	16 s	11 s	10 s	8 s	6 s	9 s	9 s

We also observed that the soliton amplitude remains stable during temporal evolution in the unidirectional case although the wavefields were propagated using the HOS method instead of the KdV equation, and intermediate waters were considered. Under increasingly directional spreading conditions, the soliton amplitude exhibits larger and larger variations during temporal evolution. Using two evaluation metrics, the Relative Error (RE) and the Relative Deviation of the Mean (RDM), we determined representative propagation times for the soliton wave heights for various significant wave heights and directional spreading conditions (see Table 2). Our results show that the largest soliton in the nonlinear spectrum is quite stable for the small directional spreading cases. However, even in cases with large directional spreading, the soliton amplitudes provided by the KdV-NFT can still retain their representative character for short propagation times or distances. These findings indicate that NFT-based analyses can be physically meaningful even under physical propagation conditions different from the integrable equation that is solved exactly by the NFT. Similar results have also been reported only recently for the deep water case, where the NFT for the nonlinear Schödinger equation is used [15].

From a practical point of view, this study provides the first attempt to quantify in particular of impact of directional spreading on nonlinear Fourier spectra obtained by applying the KdV-NFT to space series extracted from multidirectional seas. Such results are important to further interpret the results of real-world studies based on the KdV-NFT such as [10–14]. For the sea states with moderate directional spreading, the nonlinear soliton spectrum varied only moderately during evolution when considered for short enough periods of time. Since surface waves in shallow water regions are expected to experience reduced spreading compared to deep water locations due to the shallow water effects [11,69], this further enhances the potential of the KdV-NFT for field measurements. We finally remind the reader that these results are based on the nonlinear temporal evolution of JONSWAP wave fields by the HOS-Ocean model. While HOS-Ocean is a powerful model, numerical models cannot always describe the nonlinear evolution of realistic wave fields accurately. For example, the HOS-Ocean model only considers non-breaking waves propagating within a uniform water depth. Another limitation of our study is that only nonlinearities up to the third order have been considered. Furthermore, real-world wave spectra tend to be more complicated than JONSWAP spectra. Therefore, high-quality field data will be essential for future investigations into the practical applicability of the KdV-NFT.

CRediT authorship contribution statement

Yu-Chen Lee: Writing – original draft, Validation, Software, Methodology, Investigation, Formal analysis, Data curation, Conceptualization. **Sander Wahls:** Writing – review & editing, Supervision, Software, Project administration, Methodology, Funding acquisition, Formal analysis, Conceptualization.

Declaration of competing interest

The authors declare the following financial interests/personal relationships which may be considered as potential competing interests: Sander Wahls reports financial support was provided by Delft University of Technology. If there are other authors, they declare that they have no known competing financial interests or personal relationships that could have appeared to influence the work reported in this paper.

Acknowledgments

The authors thank Guillaume Ducrozet for helpful discussions about HOS-Ocean. The second author furthermore thanks Gino Biondini, who suggested to compare the evolution of the largest soliton with that of the largest linear mode (Fig. 14). The second author finally also thanks the Isaac Newton Institute for Mathematical Sciences, Cambridge, for support and hospitality during the program “Emergent phenomena in nonlinear dispersive waves” (EPSRC, United Kingdom grant EP/R014604/1), during which the discussion with Prof. Biondini took place.

All authors have read and approved the final version of the manuscript and agree to its submission to Wave Motion

Data availability

Data will be made available on request.

References

[1] J.S. Russell, Report on waves, in: Report of the Fourteenth Meeting of the British Association for the Advancement of Science, vol. 25, 1844.
[2] N.J. Zabusky, M.D. Kruskal, Interaction of" solitons" in a collisionless plasma and the recurrence of initial states, Phys. Rev. Lett. 15 (6) (1965) 240.
[3] C.S. Gardner, J.M. Greene, M.D. Kruskal, R.M. Miura, Method for solving the Korteweg-deVries equation, Phys. Rev. Lett. 19 (19) (1967) 1095.
[4] A. Osborne, Nonlinear Ocean Waves and the Inverse Scattering Transform, Academic Press, 2010.
[5] A. Osborne, M. Petti, Laboratory-generated, shallow-water surface waves: Analysis using the periodic, inverse scattering transform, Phys. Fluids 6 (5) (1994) 1727–1744.
[6] M. Brühl, H. Oumeraci, Analysis of long-period cosine-wave dispersion in very shallow water using nonlinear Fourier transform based on KdV equation, Appl. Ocean Res. 61 (2016) 81–91.
[7] S. Trillo, G. Deng, G. Biondini, M. Klein, G.F. Clauss, A. Chabchoub, M. Onorato, Experimental observation and theoretical description of multisoliton fission in shallow water, Phys. Rev. Lett. 117 (2016) 144102, http://dx.doi.org/10.1103/PhysRevLett.117.144102, URL https://link.aps.org/doi/10.1103/PhysRevLett.117.144102.
[8] M. Brühl, P.J. Prins, S. Ujvary, I. Barranco, S. Wahls, P.L.-F. Liu, Comparative analysis of bore propagation over long distances using conventional linear and KdV-based nonlinear Fourier transform, Wave Motion 111 (2022) 102905.
[9] P. de Koster, M. Brühl, S. Wahls, Water-depth identification from free-surface data using the KdV-based nonlinear Fourier transform, in: International Conference on Offshore Mechanics and Arctic Engineering, vol. 85901, American Society of Mechanical Engineers, 2022, V05BT06A056.
[10] A.R. Osborne, E. Segre, G. Boffetta, L. Cavaleri, Soliton basis states in shallow-water ocean surface waves, Phys. Rev. Lett. 67 (1991) 592–595, http://dx.doi.org/10.1103/PhysRevLett.67.592, URL https://link.aps.org/doi/10.1103/PhysRevLett.67.592.
[11] A. Osborne, M. Serio, L. Bergamasco, L. Cavaleri, Solitons, cnoidal waves and nonlinear interactions in shallow-water ocean surface waves, Phys. D: Nonlinear Phenom. (ISSN: 0167-2789) 123 (1) (1998) 64–81, http://dx.doi.org/10.1016/S0167-2789(98)00112-2, Annual International Conference of the Center for Nonlinear Studies. URL https://www.sciencedirect.com/science/article/pii/S0167278998001122.
[12] A. Costa, A.R. Osborne, D.T. Resio, S. Alessio, E. Chrivi, E. Saggese, K. Bellomo, C.E. Long, Soliton turbulence in shallow water ocean surface waves, Phys. Rev. Lett. 113 (10) (2014) 108501.
[13] I. Teutsch, M. Brühl, R. Weisse, S. Wahls, Contribution of solitons to enhanced rogue wave occurrence in shallow depths: A case study in the Southern North Sea, Nat. Hazards Earth Syst. Sci. 23 (6) (2023) 2053–2073.
[14] I. Teutsch, R. Weisse, S. Wahls, Brief communication: Implications of outstanding solitons for the occurrence of rogue waves at two additional sites in the North Sea, Nat. Hazards Earth Syst. Sci. 24 (6) (2024) 2065–2069, http://dx.doi.org/10.5194/nhess-24-2065-2024, URL https://nhess.copernicus.org/articles/24/2065/2024/.
[15] A. Slunyaev, Soliton groups and extreme wave occurrence in simulated directional sea waves, Phys. Fluids 36 (7) (2024).
[16] G. Ducrozet, F. Bonnefoy, D. Le Touzé, P. Ferrant, HOS-ocean: Open-source solver for nonlinear waves in open ocean based on high-order spectral method, Comput. Phys. Comm. 203 (2016) 245–254.
[17] V.E. Zakharov, Stability of periodic waves of finite amplitude on the surface of a deep fluid, J. Appl. Mech. Tech. Phys. 9 (2) (1968) 190–194.
[18] G. Ducrozet, F. Bonnefoy, D. Le Touzé, P. Ferrant, 3-D HOS simulations of extreme waves in open seas, Nat. Hazards Earth Syst. Sci. 7 (1) (2007) 109–122.
[19] W. Xiao, Y. Liu, G. Wu, D.K. Yue, Rogue wave occurrence and dynamics by direct simulations of nonlinear wave-field evolution, J. Fluid Mech. 720 (2013) 357–392.
[20] A. Kokorina, A. Slunyaev, Lifetimes of rogue wave events in direct numerical simulations of deep-water irregular sea waves, Fluids 4 (2) (2019) 70.
[21] E.M. Bitner-Gregersen, O. Gramstad, A.K. Magnusson, M.P. Malila, Extreme wave events and sampling variability, Ocean. Dyn. 71 (1) (2021) 81–95.
[22] C. Kirezci, A.V. Babanin, D. Chalikov, Probabilistic assessment of rogue wave occurrence in directional wave fields, Ocean. Dyn. 71 (11–12) (2021) 1141–1166.
[23] S. Davison, A. Benetazzo, F. Barbariol, G. Ducrozet, J. Yoo, M. Marani, Space-time statistics of extreme ocean waves in crossing sea states, Front. Mar. Sci. 9 (2022) 1002806.
[24] A. Slunyaev, A. Kokorina, Account of occasional wave breaking in numerical simulations of irregular water waves in the focus of the rogue wave problem, Water Waves 2 (2) (2020) 243–262.
[25] G. Ducrozet, F. Bonnefoy, Y. Perignon, Applicability and limitations of highly non-linear potential flow solvers in the context of water waves, Ocean Eng. 142 (2017) 233–244.
[26] B.R. Seiffert, G. Ducrozet, Simulation of breaking waves using the high-order spectral method with laboratory experiments: Wave-breaking energy dissipation, Ocean. Dyn. 68 (1) (2018) 65–89.
[27] D.G. Dommermuth, D.K. Yue, A high-order spectral method for the study of nonlinear gravity waves, J. Fluid Mech. 184 (1987) 267–288.
[28] B.J. West, K.A. Brueckner, R.S. Janda, D.M. Milder, R.L. Milton, A new numerical method for surface hydrodynamics, J. Geophys. Res.: Ocean. 92 (C11) (1987) 11803–11824.
[29] F. Bonnefoy, G. Ducrozet, D. Le Touzé, P. Ferrant, Time domain simulation of nonlinear water waves using spectral methods, in: Advances in Numerical Simulation of Nonlinear Water Waves, World Scientific, 2010, pp. 129–164.
[30] G. Ducrozet, H.B. Bingham, A.P. Engsig-Karup, F. Bonnefoy, P. Ferrant, A comparative study of two fast nonlinear free-surface water wave models, Internat. J. Numer. Methods Fluids 69 (11) (2012) 1818–1834.
[31] G. Ducrozet, F. Bonnefoy, P. Ferrant, Rogue waves in large-scale fully-non-linear high-order-spectral simulations, in: Proc. 22nd International Workshop on Water Waves and Floating Bodies, IWWWFB, Croatia, 2007.
[32] G. Ducrozet, M. Abdolahpour, F. Nelli, A. Toffoli, Predicting the occurrence of rogue waves in the presence of opposing currents with a high-order spectral method, Phys. Rev. Fluids 6 (6) (2021) 064803.
[33] Z. Li, G. Deng, P. Queutey, B. Bouscasse, G. Ducrozet, L. Gentaz, D. Le Touzé, P. Ferrant, Comparison of wave modeling methods in CFD solvers for ocean engineering applications, Ocean Eng. 188 (2019) 106237.
[34] Q. Xiao, R. Zhu, S. Huang, Hybrid time-domain model for ship motions in nonlinear extreme waves using HOS method, Ocean Eng. 192 (2019) 106554.
[35] J.R. Cash, A.H. Karp, A variable order Runge-Kutta method for initial value problems with rapidly varying right-hand sides, ACM Trans. Math. Softw. (TOMS) 16 (3) (1990) 201–222.
[36] A. Osborne, The inverse scattering transform: Tools for the nonlinear Fourier analysis and filtering of ocean surface waves, Chaos Solitons Fractals 5 (12) (1995) 2623–2637.
[37] T.B. Benjamin, Instability of periodic wavetrains in nonlinear dispersive systems, Proc. R. Soc. Lond. Ser. A. Math. Phys. Sci. 299 (1456) (1967) 59–76.
[38] R. Johnson, On the modulation of water waves in the neighbourhood of kh 1.363, Proc. R. Soc. A 357 (1689) (1977) 131–141.
[39] E.D. Belokolos, A.I. Bobenko, V.Z. Enolskii, A.R. Its, V.B. Matveev, Algebro-Geometric Approach to Nonlinear Integrable Equations, vol. 1994, Springer, 1994.
[40] A. Osborne, E. Segre, The numerical inverse scattering transform for the periodic Korteweg-de Vries equation, Phys. Lett. A 173 (2) (1993) 131–142.
[41] A. Osborne, L. Bergamasco, The solitons of Zabusky and Kruskal revisited: Perspective in terms of the periodic spectral transform, Phys. D: Nonlinear Phenom. 18 (1–3) (1986) 26–46.
[42] A. Osborne, Soliton physics and the periodic inverse scattering transform, Phys. D: Nonlinear Phenom. 86 (1–2) (1995) 81–89.

[43] S. Wahls, S. Chimmalgi, P.J. Prins, FNFT: A software library for computing nonlinear Fourier transforms, J. Open Source Softw. 3 (23) (2018) 597.
[44] S. Wahls, H.V. Poor, Fast inverse nonlinear Fourier transform for generating multi-solitons in optical fiber, in: 2015 IEEE International Symposium on Information Theory, ISIT, IEEE, 2015, pp. 1676–1680.
[45] S. Wahls, Fiber-optic communication using fast nonlinear Fourier transforms, in: 2016 Optical Fiber Communications Conference and Exhibition, OFC, IEEE, 2016, pp. 1–3.
[46] P. De Koster, S. Wahls, Dispersion and nonlinearity identification for single-mode fibers using the nonlinear Fourier transform, J. Lightwave Technol. 38 (12) (2020) 3252–3260.
[47] S. Wahls, M. Bruehl, Y.-M. Fan, C.-J. Huang, Nonlinear fourier analysis of free-surface buoy data using the software library fnft, in: International Conference on Offshore Mechanics and Arctic Engineering, vol. 84386, American Society of Mechanical Engineers, 2020, V06BT06A070.
[48] Y.-C. Lee, S. Wahls, M. Brühl, Evaluation of nonlinear Fourier-based maximum wave height predictors under the nonlinear Schrödinger equation, in: International Conference on Offshore Mechanics and Arctic Engineering, vol. 85901, American Society of Mechanical Engineers, 2022, V05BT06A060.
[49] Y.-C. Lee, M. Brühl, D.-J. Doong, S. Wahls, Nonlinear Fourier classification of 663 rogue waves measured in the philippine sea, PLoS One 19 (5) (2024) e0301709.
[50] M.S. Longuet-Higgins, Observation of the directional spectrum of sea waves using the motions of a floating buoy, Oc. Wave Spectra (1963).
[51] V.S. Kumar, M. Deo, N. Anand, P. Chandramohan, Estimation of wave directional spreading in shallow water, Ocean Eng. 26 (1) (1998) 83–98.
[52] M. Miche, Mouvements ondulatoires de la mer en profondeur constante ou décroissante, Ann. Ponts Chaus. (1944) 1944, Pp (1) 26- 78, (2) 270- 292, (3) 369- 406.
[53] B. Ruessink, D. Walstra, H. Southgate, Calibration and verification of a parametric wave model on barred beaches, Coast. Eng. 48 (3) (2003) 139–149.
[54] W. Rattanapitikon, Calibration and modification of energy dissipation models for irregular wave breaking, Ocean Eng. 34 (11–12) (2007) 1592–1601.
[55] W. Rattanapitikon, Verification of significant wave representation method, Ocean Eng. 35 (11–12) (2008) 1259–1270.
[56] R.G. Dean, R.A. Dalrymple, Water Wave Mechanics for Engineers and Scientists, vol. 2, world scientific publishing company, 1991.
[57] Z.-J. You, A close approximation of wave dispersion relation for direct calculation of wavelength in any coastal water depth, Appl. Ocean Res. 30 (2) (2008) 113–119.
[58] A. Toffoli, M. Benoit, M. Onorato, E. Bitner-Gregersen, The effect of third-order nonlinearity on statistical properties of random directional waves in finite depth, Nonlinear Process. Geophys. 16 (1) (2009) 131–139.
[59] D. Dommermuth, The initialization of nonlinear waves using an adjustment scheme, Wave Motion 32 (4) (2000) 307–317.
[60] A. Slunyaev, A. Kokorina, Numerical simulation of the sea surface rogue waves within the framework of the potential Euler equations, Izv. Atmos. Ocean. Phys. 56 (2020) 179–190.
[61] I.-C. Kim, G. Ducrozet, V. Leroy, F. Bonnefoy, Y. Perignon, S. Delacroix, Numerical and experimental investigation on deterministic prediction of ocean surface wave and wave excitation force, Appl. Ocean Res. 142 (2024) 103834.
[62] P.A. Janssen, Nonlinear four-wave interactions and freak waves, J. Phys. Oceanogr. 33 (4) (2003) 863–884.
[63] N. Mori, P.A. Janssen, On kurtosis and occurrence probability of freak waves, J. Phys. Oceanogr. 36 (7) (2006) 1471–1483.
[64] A. Toffoli, M. Onorato, A. Osborne, J. Monbaliu, Non-Gaussian properties of shallow water waves in crossing seas, Extrem. Ocean. Waves (2008) 53–69.
[65] E. Pelinovsky, A. Sergeeva, Numerical modeling of the KdV random wave field, Eur. J. Mech. B Fluids 25 (4) (2006) 425–434.
[66] T.A. Driscoll, N. Hale, L.N. Trefethen, Chebfun guide, 2014.
[67] J. Boussinesq, Théorie de l'intumescence liquide appelée onde solitaire ou de translation se propageant dans un canal rectangulaire, CR Acad. Sci. Paris 72 (755–759) (1871) 1871.
[68] J.W. Miles, Solitary waves, Annu. Rev. Fluid Mech. 12 (1) (1980) 11–43.
[69] G.Z. Forristall, K.C. Ewans, Worldwide measurements of directional wave spreading, J. Atmos. Ocean. Technol. 15 (2) (1998) 440–469.